actuators

MDPI

Article

# Optimal Design of a Surface Permanent Magnet Machine for Electric Power Steering Systems in Electric Vehicle Applications Using a Gaussian Process-Based Approach

**Gilsu Choi [1], Gwan-Hui Jang [1], Mingyu Choi [1,†], Jungmoon Kang [1], Ye Gu Kang [2,*] and Sehwan Kim [3]**

[1] Department of Electrical and Computer Engineering, Inha University, Incheon 22212, Republic of Korea; gchoi@inha.ac.kr (G.C.); jkh9452@inha.edu (G.-H.J.); mingyu5832@inha.edu (M.C.); jmkang@inha.edu (J.K.)
[2] School of Electrical, Electronics & Communication Engineering, Korea University of Technology and Education, Cheonan 31253, Republic of Korea
[3] Korea Institute of Machinery and Materials, Pusan 46744, Republic of Korea; sehwan@kimm.re.kr
* Correspondence: kang@koreatech.ac.kr
† Graduated.

**Abstract:** The efficient design optimization of electric machines for electric power steering (EPS) applications poses challenges in meeting demanding performance criteria, including high power density, efficiency, and low vibration. Traditional optimization approaches often fail to find a global solution or suffer from excessive computation time. In response to the limitations of traditional approaches, this paper introduces a novel methodology by incorporating a Gaussian process-based adaptive sampling technique into a surrogate-assisted optimization process using a metaheuristic algorithm. Validation on a 72-slot/8-pole interior permanent magnet (IPM) machine demonstrates the superiority of the proposed approach, showcasing improved exploitation–exploration balance, faster convergence, and enhanced repeatability compared to conventional optimization methods. The proposed design process is then applied to two surface PM (SPM) machine configurations with 9-slot/6-pole and 12-slot/10-pole combinations for EPS applications. The results indicate that the 12-slot/10-pole SPM design surpasses the alternative design in torque density, efficiency, cogging torque, torque ripple, and manufacturability.

**Keywords:** design optimization; electric machines; electric power steering systems; electric vehicles; gaussian process; adaptive sampling

check for updates

**Citation:** Choi, G.; Jang, G.-H.; Choi, M.; Kang, J.; Kang, Y.G.; Kim, S. Optimal Design of a Surface Permanent Magnet Machine for Electric Power Steering Systems in Electric Vehicle Applications Using a Gaussian Process-Based Approach. *Actuators* **2024**, *13*, 13. https://doi.org/10.3390/act13010013

Academic Editor: Dong Jiang

Received: 6 December 2023
Revised: 26 December 2023
Accepted: 28 December 2023
Published: 29 December 2023



## 1. Introduction

In the era of electric mobility, the pursuit of efficient and high-performance electric power steering (EPS) systems has become central to the evolution of vehicular dynamics. The electric machine, at the heart of these systems, plays a pivotal role in converting electrical energy into precise mechanical assistance. Electric machines for EPS systems are required to meet demanding performance requirements, including high power density, efficiency, low noise and vibration, and fault tolerance [1]. Additionally, compactness and lightweight characteristics are essential for seamless integration into vehicles without compromising space or adding excessive weight.

Addressing specific design goals, such as the reduction of torque ripple and cogging torque, becomes crucial as the rotating movement is converted into the linear movement of the steering rack [2,3]. These factors directly impact the vibration and overall driving comfort of the vehicle. Ensuring fault tolerance is equally important to guarantee continued system functionality after a failure [4]. As electric vehicles (EVs) become mainstream, optimizing the performance characteristics of EPS machines has become critical. However, the limitations of traditional machine design approaches are becoming apparent, necessitating more powerful and efficient design methodologies.

Rotating electrical machines, due to their complex geometry and nonlinear magnetic saturation characteristics, are often designed using numerical methods like Finite Element Analysis (FEA) rather than analytical approaches. While computer simulations such as FEA aid in the design process, the optimization of electrical machines for varying performance characteristics poses challenges. These challenges include multi-variable and multi-objective optimization problems requiring exploration of the entire design space. However, the computational expense associated with FEA makes full design space exploration impractical, particularly as the number of design variables increases [5–9].

In response to the limitations of conventional optimization approaches, recent years have seen active research in metaheuristic, algorithm-based machine design optimization. Techniques utilizing genetic algorithms, particle swarm optimization, and similar methods based on FEA have been explored. Although these metaheuristic algorithms offer optimal solutions, they demand substantial computations, resulting in significant computation time. To address this, recent studies have investigated surrogate-assisted metaheuristic algorithms [10,11]. The approach exemplified in [11] proposes a systematic design optimization process for internal permanent magnet synchronous machines (IPMSMs), utilizing surrogate models (SMs), such as Kriging, artificial neural networks (ANNs), and support vector regression (SVM). While these approaches significantly reduce computation time without compromising accuracy, the selection of effective samples for SM construction and evolutionary search algorithms has not yet been fully discussed.

The accuracy and efficiency of SM is closely related to the quality and quantity of the dataset used for training [12–14]. For optimal design, the training dataset must be representative of the entire input space to avoid bias and allow the surrogate model to generalize well [15–17]. Despite the critical role of dataset selection, comprehensive discussions on optimizing the data selection strategy for efficiency and fast convergence are lacking in past literature on electric machine design. This paper addresses this imperative challenge by introducing a cutting-edge approach: application of Gaussian process-based algorithms for the optimal design of EPS machines.

The Gaussian process (GP), known for its ability to model complex and nonlinear relationships, provides a promising avenue for systematically exploring the design space. Its objective, in the context of electric machine design, is to identify design configurations that maximize power density while enhancing overall performance. This paper provides a systematic and detailed description of how the GP can be integrated into surrogate-assisted optimization techniques using metaheuristic algorithms to develop an efficient design optimization process. The major contributions of this paper are outlined as follows:

- Development of a design optimization process utilizing adaptive sampling that blends exploitation and exploration to simultaneously improve model accuracy and convergence speed.
- Validation of the developed optimization process through its application to a 72-slot/8-pole IPMSM for traction applications.
- Comprehensive design and analysis of surface permanent magnet (SPM) machines to address design challenges for EPS applications.
- Comparative analysis and design optimization of two promising PM machine topologies: SPM machines equipped with fractional-slot concentrated windings (FSCW) with 9-slot/6-pole and 12-slot/10-pole.
- Experimental verification of the optimal design through the construction and testing of a prototype machine.

The subsequent sections of this paper are organized as follows: Section 2 provides an overview of the Gaussian process-based adaptive sampling algorithm proposed in this paper and presents validation results on the performance of the proposed algorithm through a case study. Details on the chosen baseline machine topologies for an EPS application and their basic electromagnetic performance are presented in Section 3. Section 4 describes a design optimization process utilizing the proposed adaptive sampling technique to find the global optimal solution for an EPS motor. Section 4 also presents the results of the

comparative study in which the proposed optimization process is applied to two promising machine configurations. Finally, experimental verification results for the final optimized design are presented in Section 5 by comparing the measured machine performance with FE predictions.

## 2. Gaussian Process-Based Adaptive Sampling Algorithm

The Gaussian Process (GP), also known as the Kriging method, serves as an interpolation technique for predicting data in a high-dimensional space based on input and output data. Widely applied in the design optimization of electrical machines, the GP algorithm significantly reduces computational time by constructing surrogate models from pre-computed simulation results, especially beneficial for extensive nonlinear numerical calculations. Recent research has concentrated on building surrogate models that ensure required accuracy with minimal computation, emphasizing the efficacy of surrogate-based optimization (SBO) with adaptive sampling for efficient and accurate design exploration.

Adaptive sampling, a pivotal technique in optimization processes, iteratively refines the surrogate model by strategically introducing new samples into crucial regions of the design space. This refinement, guided by response surface information from the existing surrogate model, facilitates the efficient construction of surrogate models, enabling improved accuracy with reduced sample size and calculation time. Two primary techniques for sample selection criteria, exploitation and exploration, play essential roles in optimizing the efficiency of the process [18].

Exploitation involves generating the next sample by identifying the point predicted as the best value of the function based on given information, employing techniques like K-fold cross-validation [19,20] and leave-one-out cross validation (LOOCV) [21]. Figure 1a shows an example of a case where additional sampling using an exploit (yellow dots) is applied. The advantage of using this technique is that it allows for efficient design space exploration to improve sample distribution and reduce the time spent searching for the optimal point. [22]. However, caution is necessary to avoid overlooking the space of interest.

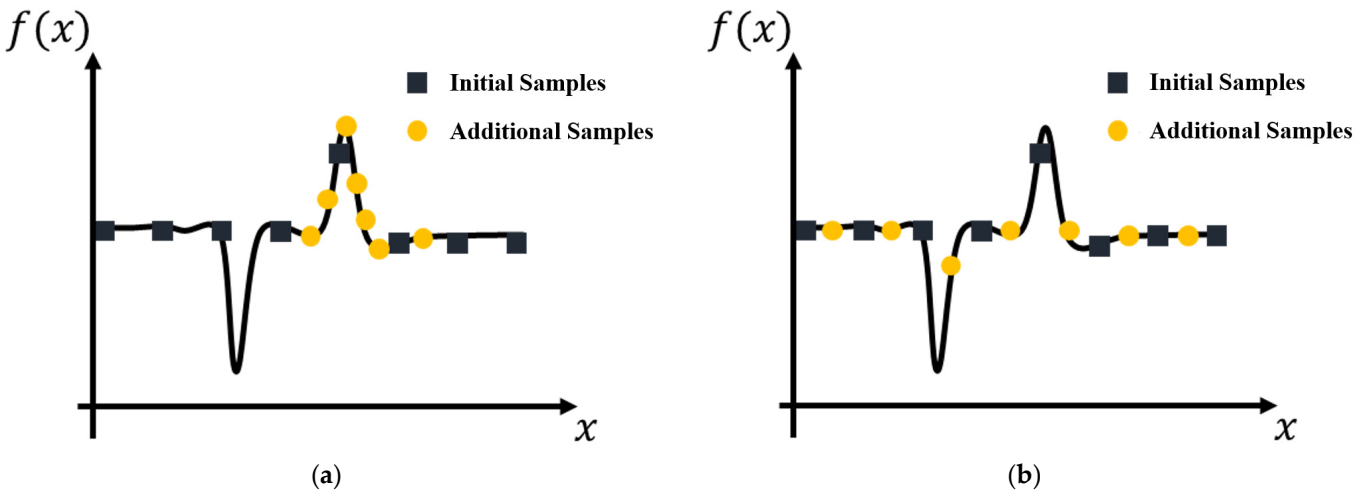


**Figure 1.** Comparison of additional sampling cases. (**a**) Case 1: Application of the exploitation, (**b**) Case 2: Application of the exploration.

On the other hand, exploration generates subsequent samples to gather information from the design space with large variance or empty space that may lead to better results. Figure 1b shows an example of additional sampling using exploration. Techniques based on the distance between samples [23,24], the variance of samples [25–27], and space-filling [28] are widely used in exploration due to their advantages in reducing uncertainty and improving the prediction accuracy of surrogate models. However, the computational burden may increase if samples are created in unnecessary space.

The paper addresses the exploitation–exploration tradeoff, a significant challenge in multi-variable, multi-objective optimization problems. Various adaptive sampling algorithms have been proposed to solve this problem, including expected improvement (EI), probability of improvement (PI), and upper confidence bound (UCB). Among them, we chose the Gaussian process-based UCB (GP-UCB) sampling method, which employs an efficient sampling approach with flexible parameter tuning capabilities to enhance the accuracy of surrogate models and improve the optimization efficiency.

The GP-UCB-based adaptive sampling proposed in this paper generates the next sample from data with the largest sum of mean and variance, as shown by the yellow line in Figure 2. The GP-UCB function $U(x)$ for an input variable $x$ can be expressed as follows [29]:

$$U(x) = \mu(x) + \kappa\sigma(x) \tag{1}$$

where $\mu(x)$ is the mean value calculated by GP regression, $\sigma(x)$ is the variance, and $\kappa$ is a hyperparameter to control the characteristics of the confidence bounds. The larger the hyperparameter, the larger the upper bound, and the algorithm favors solutions that explore currently unexplored regions of the design space. On the other hand, when κ is small, the algorithm focuses more on finding high-performance solutions.

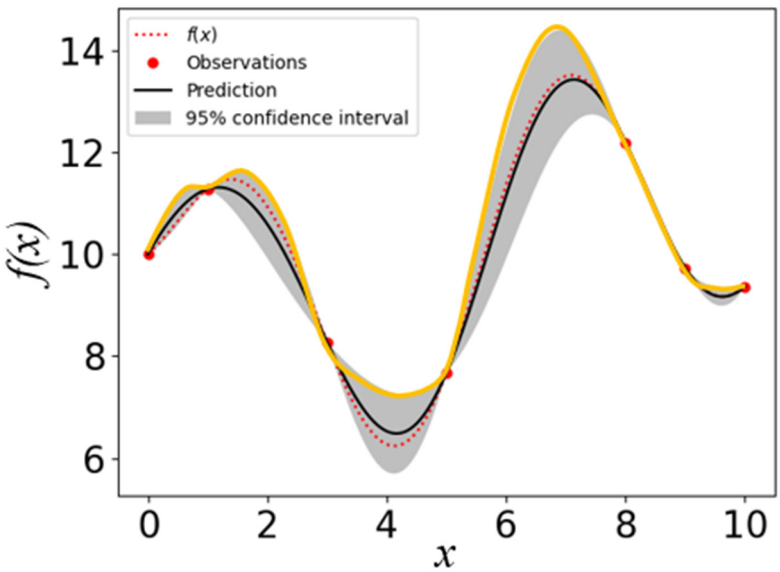


**Figure 2.** Illustration of the input–output relationship of the Gaussian process and GP-UCB (yellow line).

When tackling problems involving one-dimensional design variables, the sampling process is straightforward, involving the computation of responses across the entire design space. However, in electric machine design, the abundance of design variables gives rise to the "curse of dimensionality", rendering exhaustive exploration of the entire design space excessively computationally time-consuming. Additionally, electric motors designed for e-mobility applications commonly involve multiple objective functions, including torque, mass, cost, and efficiency. In the following sections, the application of the proposed GP-UCB-based design optimization process to two case studies will be presented, effectively delivering a comprehensive optimal solution to multi-objective, multi-variable problems.

### *2.1. Proposed Optimization Process*

Figure 3 presents a comparative analysis between the conventional SM-based optimization process and the proposed optimization process employing the GP-UCB-based adaptive sampling technique. Both methods start with initial samples generated via a design of experiment (DOE) technique to construct an initial surrogate model, approximating the performance response of the electric machine under consideration. In the traditional approach depicted in Figure 3a, the prediction results of the SM model are iteratively

compared with FE calculation results, and the calculated FEA results are incorporated into the model training set to enhance accuracy until convergence criteria are met. In contrast, as illustrated in Figure 3b, the proposed technique leverages GP-UCB and a metaheuristic algorithm to identify the Pareto front for the given objective function. This information is then utilized to generate the subsequent dataset for SM training. However, it is acknowledged that GP-UCB predictions may encounter local minima due to approximation errors. To avoid this challenge, the proposed optimization process integrates a space-filling technique to generate additional samples from undiscovered regions. This has a similar effect to mutation in a genetic algorithm.

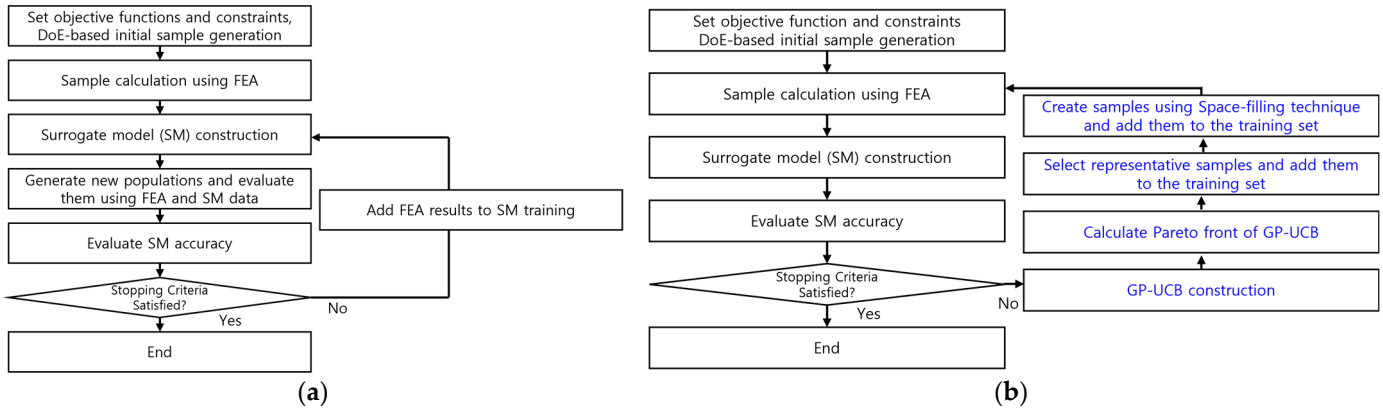


**Figure 3.** Comparison of the flowcharts. (**a**) Conventional optimization process, (**b**) proposed GP-UCB-based optimization process.

### *2.2. Case Study: 72-Slot/8-Pole IPM Traction Machine*

This section presents the results of the case study conducted to validate the performance of the proposed adaptive sampling algorithm. The chosen reference model is an interior permanent magnet synchronous machine (IPMSM) originally designed in [30], featuring 72 slots, 8 poles, and hairpin windings on the stator. The choice of this reference model was based on the recognition that the proposed optimization process may not perform well when faced with very complex datasets. IPMSMs are known to be challenging to model, with significant nonlinearities due to deep magnetic saturation. Figure 4 shows a cross-section of the baseline IPMSM with key design parameters, and Table 1 provides information on the key parameters of the reference motor.

The two objective functions for this case study are the torque density of the machine and the total active material cost, which are expressed as follows:

$$\text{minimize:} \quad \begin{array}{l} 1.\ -(Tpk/m_{total})\ [\text{Nm/kg}] \\ 2.\ \text{Active material cost [\$]} \end{array}$$

where $Tpk$ is the peak torque and $m_{total}$ is the total mass of active materials. The assumed material costs are \$2.36/kg for the iron core, \$118/kg for magnets, and \$9.44/kg for copper.

**Table 1.** Main parameters of the 72-slot/8-pole IPMSM motor.

| Parameter | Value |
|---|---|
| Slot/Pole | 72/8 |
| Peak current density | 25 Arms/mm$^2$ |
| Maximum current | 400 Arms |
| Airgap length | 0.75 mm |
| Rotor outer diameter | 150 mm |
| Stator outer diameter | mm |
| Stack length | 90 mm |

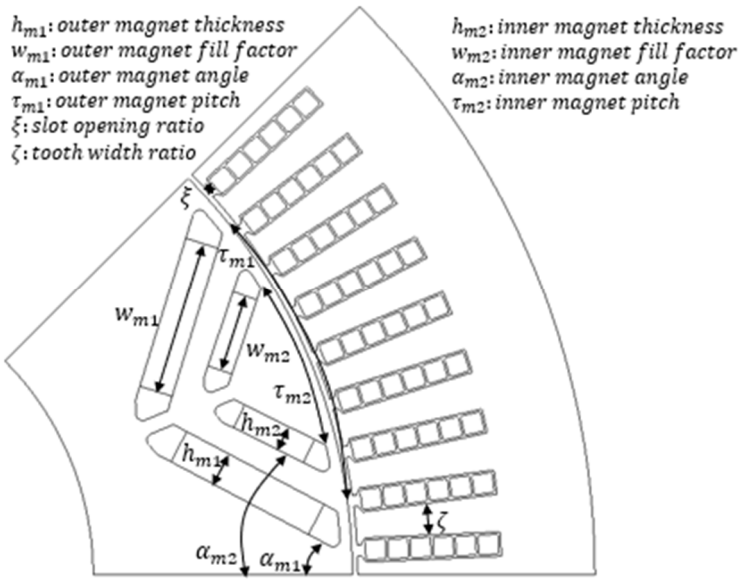


**Figure 4.** Cross section of the 72-slot/8-pole IPMSM baseline model.

To assess the efficacy of the proposed algorithm, critical performance metrics are examined, including exploitation–exploration balance, convergence speed, sensitivity to initial sampling, and repeatability. The SM is established using the GP-based algorithm detailed in [11], with NSGA-II employed for metaheuristic optimization. NSGA-II parameters include a crossover probability of 0.9 and a mutation probability of 0.05. The hyperpameter for GP-UCB is set to 1, and root-mean-square-error (*RMSE*) serves as a key metric, comparing SM and FEA results and acting as a convergence criterion. The mathematical expression of *RMSE* can be written as:

$$RMSE = \sqrt{\frac{1}{n}\sum_{i=1}^{n}(y_i - \hat{y}_i)} \times 100\% \tag{2}$$

where $y_i$ is the $i$th data calculated using FEA, and $\hat{y}_i$ is the predicted value by SM.

Convergence occurs when the *RMSE* value is less than 0.5% of the average of the results of all accumulated FEA calculations. This can be expressed as follows:

$$RMSE \leq \frac{1}{n}\sum_{i=1}^{n} y_i \times 0.5\% \tag{3}$$

The adaptive sampling technique aims to optimize a balance between exploitation and exploration, promoting comprehensive exploration while exploiting regions likely to contain optimal solutions. Figure 5 compares exploitation–exploration balance among three sampling techniques: Latin hypercube sampling (LHS), NSGA-II, and the proposed GP-UCB-based adaptive sampling. Figure 5d demonstrates superior performance of the GP-UCB-based method, enhancing the Pareto front and concentrating sample distribution near it, with the same number of the initial 200 samples. Alternatively, if fewer samples are used in the GP-UCB-based method, similar performance can still be achieved compared to the other two techniques.

Furthermore, the proposed GP-UCB-based method exhibits accelerated convergence, as shown in Figure 6. During the first iteration with 50 samples, *RMSE* values for the GP-UCB-based method (0.57%) outperform those for the other methods (1.42% and 2.25%). In fact, the *RMSE* value of the GP-UCB method almost satisfies the predefined convergence condition in (2) in one iteration. This improved convergence speed is attributed to the adaptive sampling technique prioritizing regions with high uncertainty or sensitivity, refining the surrogate model more rapidly. Consequently, the GP-UCB-based adaptive

sampling demonstrates robustness across multiple optimization runs by reducing the sensitivity to the quality of the initial sample generated by random sampling techniques such as LHS.

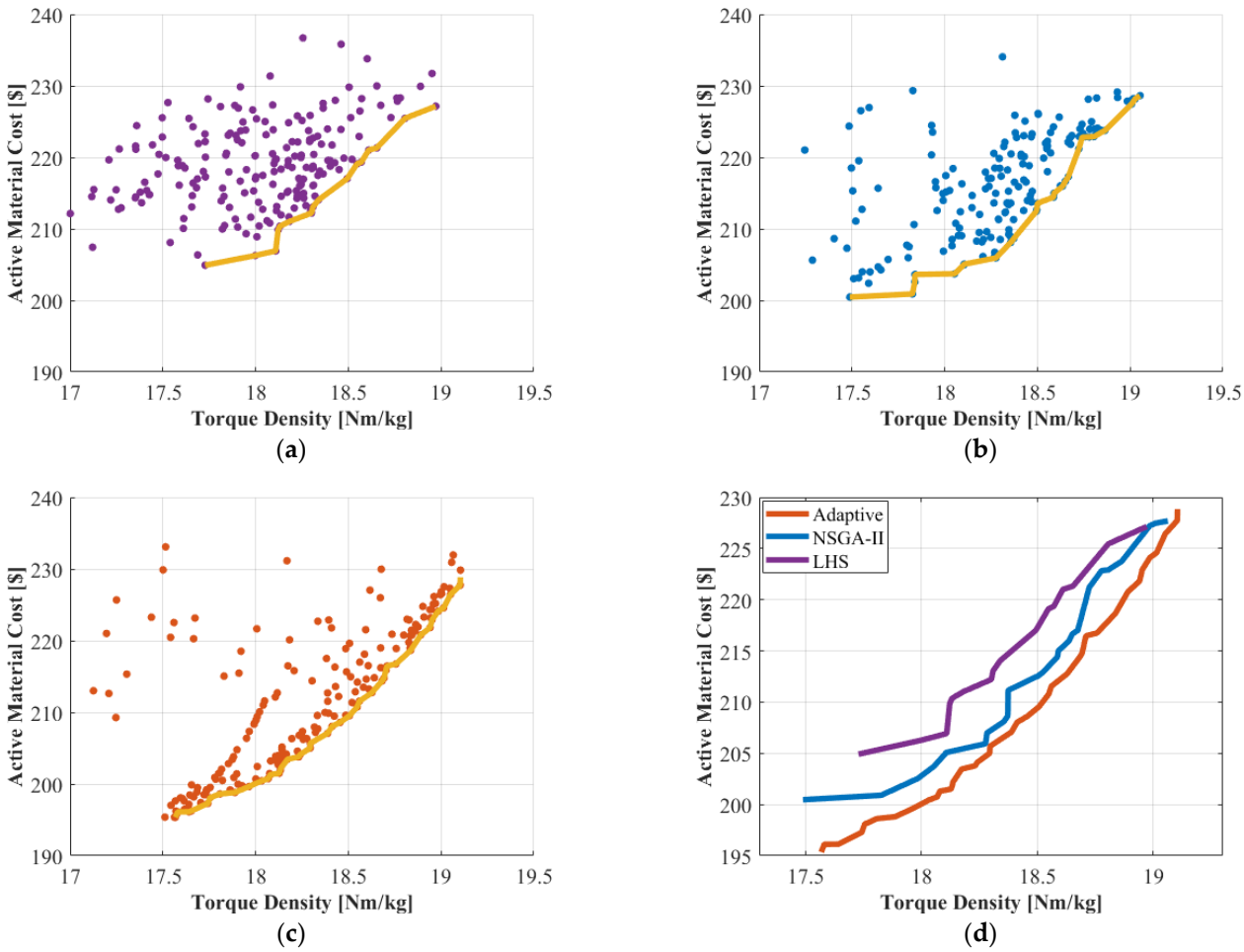


**Figure 5.** Comparison of exploitation–exploration balance. (**a**) Sample distribution using LHS, (**b**) sample distribution using NSGA-II, (**c**) sample distribution using GP-UCB, (**d**) comparison of Pareto fronts. (dots: Pareto dominated solutions, lines: Pareto fronts).

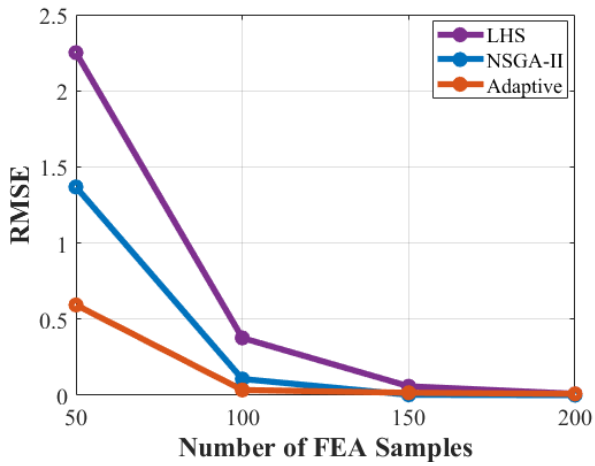


**Figure 6.** Comparison of convergence speed.

The performance of the optimization process can vary depending on the initial sample distribution [31]. Figure 7 illustrates the distribution and initial Pareto front of samples generated from five independent runs of LHS. Performing optimizations for each dataset generated by the random sampling technique can lead to repeatability issues. The proposed GP-UCB-based optimization method helps to mitigate this repeatability problem by striking an exploration–development balance to rapidly improve model accuracy and convergence speed. Figure 8 shows that the GP-UCB-based adaptive sampling proved to be robust, with nearly identical Pareto front results across the five optimization runs.

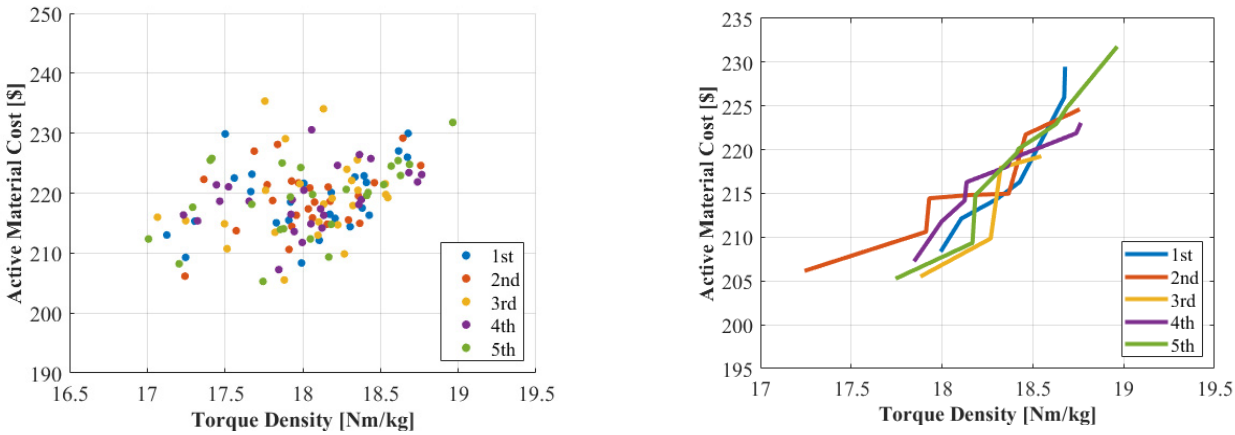


(**a**) (**b**)

**Figure 7.** Sensitivity to initial sampling. (**a**) Data distribution after 5 initial sampling runs (50 sample generation), (**b**) Pareto fronts comparison.

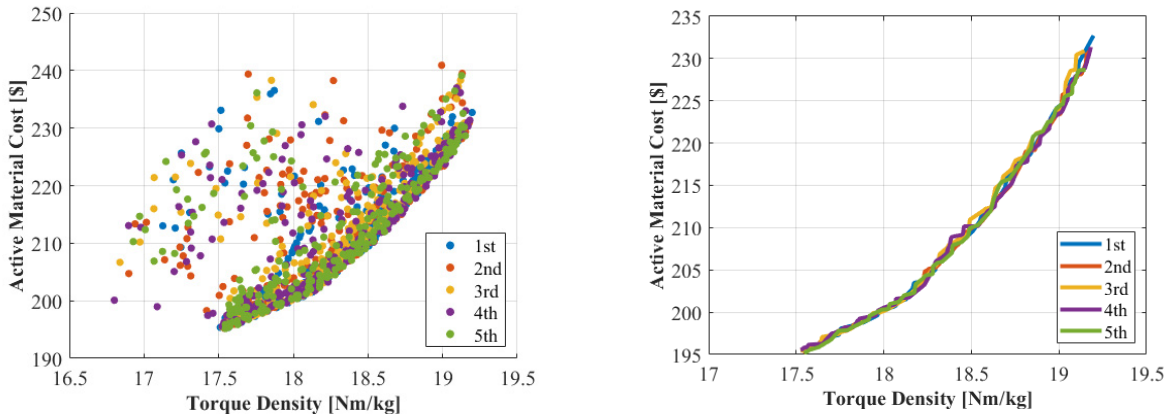


(**a**) (**b**)

**Figure 8.** Repeatability comparison between five simulation runs. (**a**) Sample distribution, (**b**) Pareto fronts comparison (the number of generations is 5, with 50 samples per generation).

In summary, the proposed GP-UCB-based adaptive sampling technique outperforms traditional methods, offering enhanced exploration of the design space, improved exploitation–exploration balance, faster convergence, reduced sensitivity to initial samples, and improved repeatability that is evident in nearly identical Pareto fronts across multiple optimization runs.

## 3. EPS Motor Design

Permanent magnet synchronous machines (PMSMs) with fractional-slot concentrated windings (FSCWs) have gained significant attention over the past two decades, driven by their advantages in power density, efficiency, and fault tolerance [32–34]. This section explores two distinct FSCW-PMSM design families characterized by slot-per-pole-per-phase

ratios of 1/2 and 2/5 for EPS applications. The 1/2 family is favored for its low harmonic contents in stator MMFs, resulting in minimal rotor losses. However, it exhibits a relatively low fundamental winding factor of 0.866. Conversely, the 2/5 family, with a fundamental winding factor ($k_{w1}$) of 0.933 and a least common multiple (LCM) value of 60, offers high torque density and low cogging torque. In particular, the 2/5 family further increases the winding factor to 0.966 when applying single-layer windings, and provides fault tolerance capability due to zero mutual coupling between phases. For balanced torque performance and machine losses, the 2/5 family with a double-layer winding configuration is selected for comparison. The two baseline designs with surface-mounted magnets (SPMs) on a rotor, featuring 9-slot/6-pole and 12-slot/10-pole combinations, are illustrated in Figure 9, with key parameters summarized in Table 2.

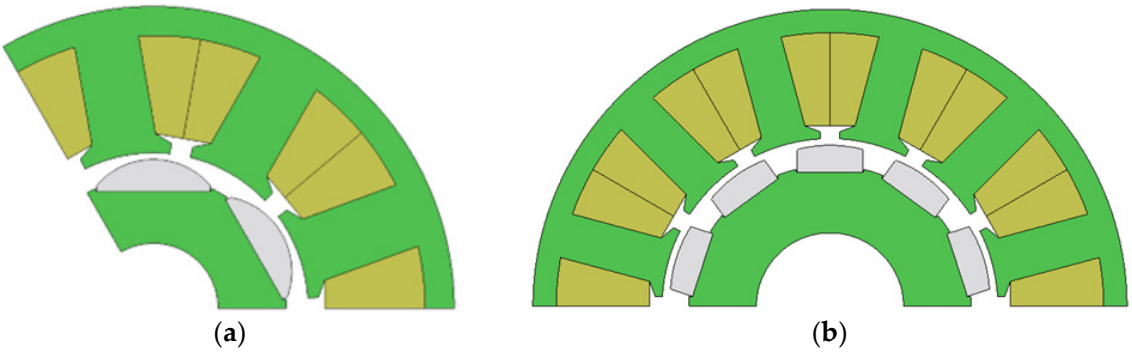


**Figure 9.** Cross-sections of the baseline designs. (**a**) Design 1: 9-slot/6-pole, (**b**) Design 2: 12-slot/10-pole.

**Table 2.** Key machine parameters for the two baseline designs.

| Parameter | Design 1 | Design 2 |
|---|---|---|
| Slot/Pole | 9/6 | 12/10 |
| DC bus voltage | 48 V | |
| Rated current | 7.57 Arms | |
| Stator diameter | 86 mm | 85 mm |
| Rotor diameter | 44 mm | 47 mm |
| Stack length | 37 mm | 36 mm |
| Series turns | 105 | 100 |
| # of parallel circuit | 3 | 2 |
| Rotor skew | Yes | No |
| Current density | 6.54 Arms/mm$^2$ | 6.36 Arms/mm$^2$ |

The stator design variables to be optimized consist of slot width ratio *bs*, slot opening ratio *bo*, and tooth-tip thickness *htt*, as shown in Figure 10a. Among these, the slot width ratio and slot height were determined, considering a given number of winding turns and current density level. The current density level was set to around 6.5 Arms/mm$^2$ at rated conditions, assuming the motor is air-cooled. The rotor design variables shown in Figure 10a, such as magnet arc eccentricity radius *rec*, magnet thickness *hpm*, and magnet width ratio $\tau pm$, were also optimized for optimal machine performance. The protruding rotor caps between the magnets prevent magnet displacement during rotor rotation. The cap structure can be categorized as rectangular or round, as shown in Figure 10b. The rotor magnets were designed in a breadloaf shape to produce near-sinusoidal back-emf waveforms to reduce cogging torque and torque ripple. The key operating points considered for optimization are shown in Table 3.

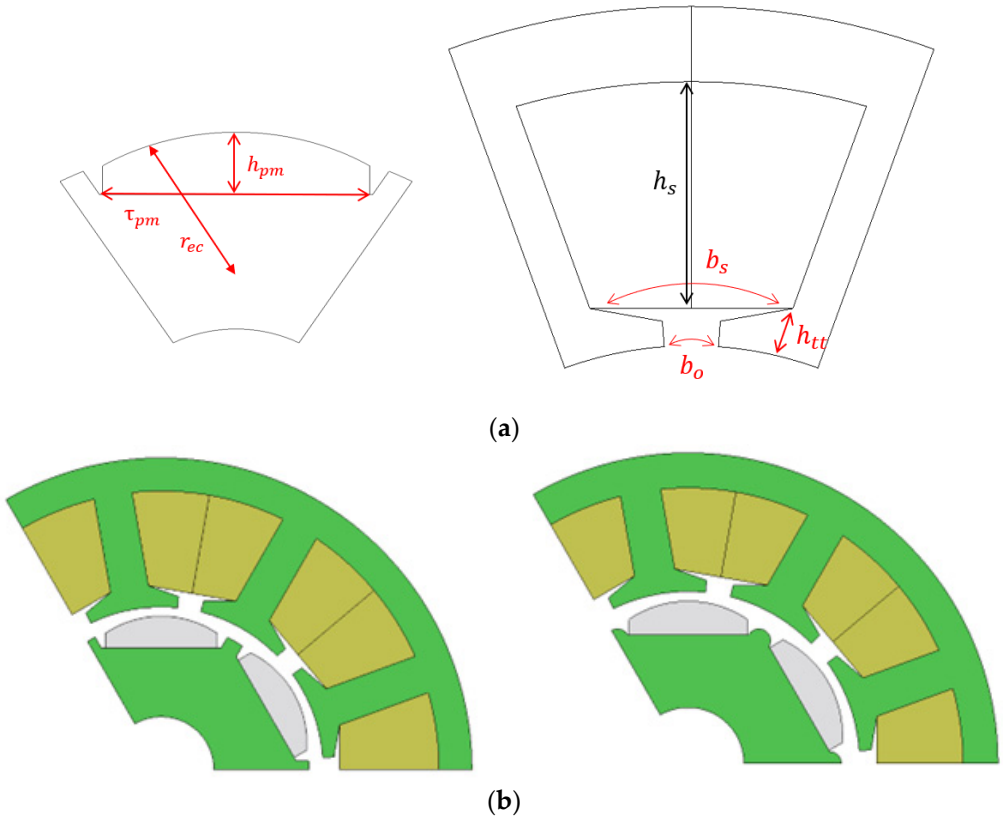


**Figure 10.** Key design variables. (**a**) Key stator and rotor variables, (**b**) rectangular cap (**left**) and round cap (**right**).

**Table 3.** Key operating points considered for optimization.

| Operating Point | Torque [Nm] | Speed [r/min] | Power [W] |
|---|---|---|---|
| Point 1 | 1.9 | 790 | 157 |
| Point 2 | 1.1 | 1750 | 202 |

As discussed extensively in previous literature, mitigating cogging torque and torque ripple in EPS motors is essential to prevent degradation of driving performance and ride quality. In this section, we conduct a comprehensive comparison of fundamental electromagnetic performance metrics, including back-emf voltage, cogging torque, and torque ripple, for the 9-slot/6-pole machine (Design 1) illustrated in Figure 9a. Figure 11 compares the back-emf waveforms and FFT spectrum for Design 1 with and without rotor skewing and rotor caps. Rotor skewing is observed to diminish the amplitude of back-emf voltage while concurrently reducing harmonic components, as shown in Figure 11b. While this reduction has a negative impact on the average torque, it is more desirable to minimize back-emf harmonics, which are a major source of torque ripple in EPS motor applications. Figure 12a further compares torque waveforms of Design 1 with and without rotor skewing and rotor cap structure under the rated load condition. Consistent with the cogging torque results in Figure 12b, rotor skewing demonstrates a reduction in both average torque and torque ripple.

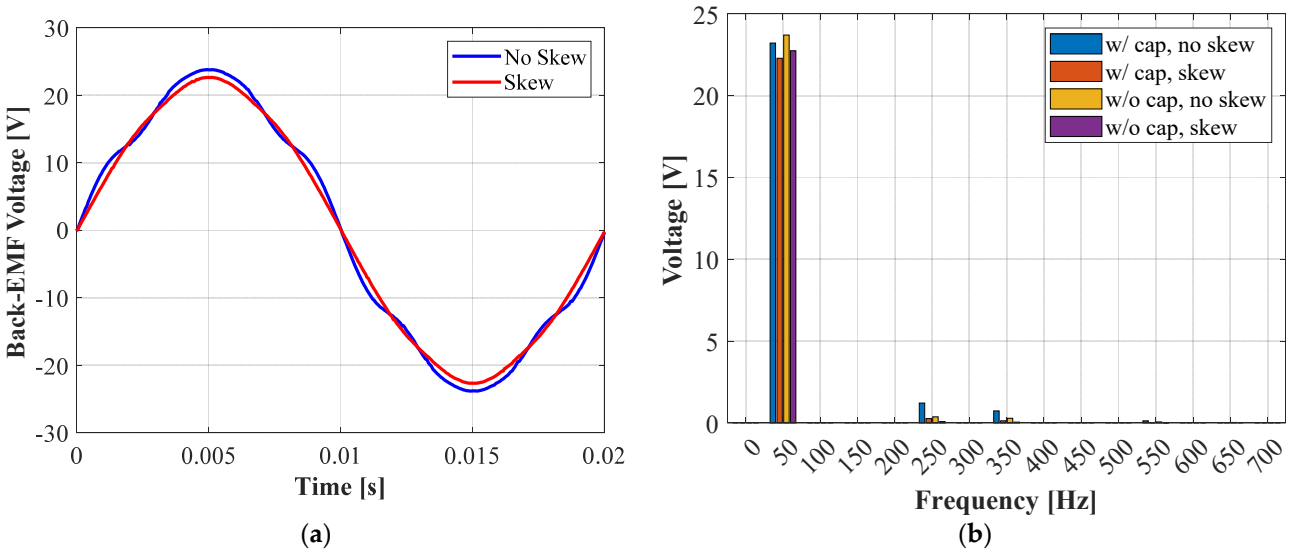


**Figure 11.** Back-emf voltage waveforms of 9-slot/6-pole design at 1000 r/min. (**a**) Back-emf waveforms comparison with and without rotor skewing, (**b**) FFT spectrum.

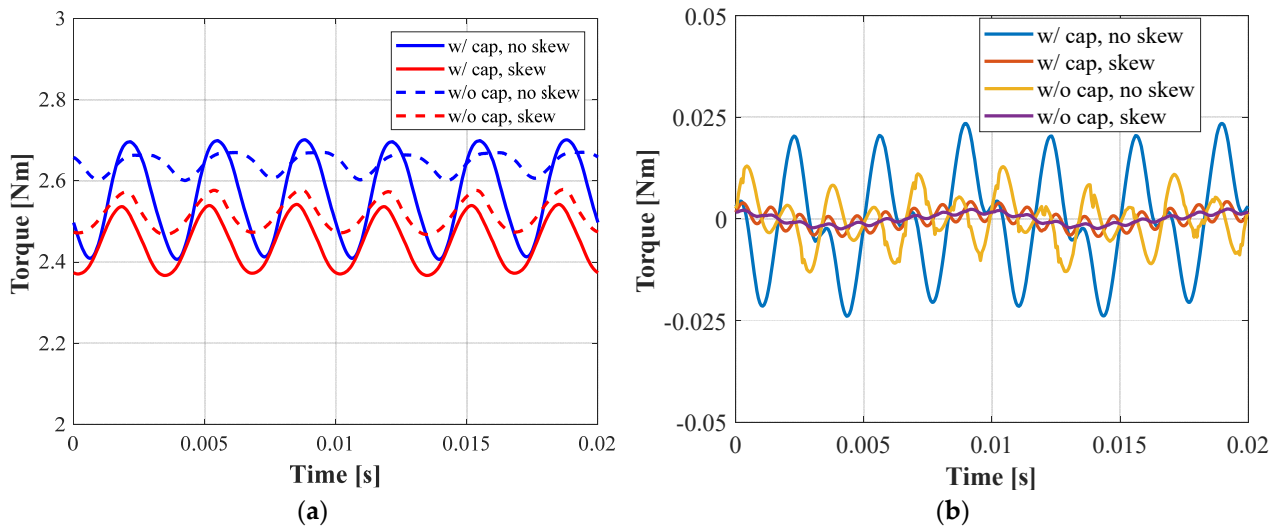


**Figure 12.** Cogging torque comparison of 9-slot/6-pole design with and without skewing and rotor cap at 790 r/min. (**a**) Instantaneous torque waveforms at rated load, (**b**) cogging torque waveforms comparison.

Figure 12 compares the cogging torque waveform with the torque waveform under the rated load condition at 790 r/min. The results in Figure 12b show that rotor skewing significantly reduces the cogging torque amplitude by a factor of 5, regardless of the presence of the rotor cap. The rotor cap, which acts as a magnet stopper, contributes to increasing the cogging torque amplitude. To balance structural and electromagnetic considerations, the height of the rotor cap is optimized to 0.5 mm. To optimize the efficacy of rotor skewing, we chose a skew step number of 3 and a 40/3° skew angle to minimize the fundamental component of the cogging torque.

## 4. Design Optimization

This section provides a detailed analysis of the results of applying the multi-objective, multi-variable design optimization process with GP-UCB-based adaptive sampling described in Section 2 to find the global optimal solution for the EPS motor.

The optimization process can be expressed as follows:

| | |
|---|---|
| minimize: | 1. $-(Tpk/m_{total})$ [Nm/kg]<br>2. Ploss [W]<br>3. Tcog [Nm] |
| subject to: | 1. Active material cost $\leq$ \$20<br>2. $Tripple \leq 4\%$ |

where Ploss is the sum of the machine losses calculated at Point 1 and 2 (see Table 3), *Tcog* is the cogging torque, and *Tripple* is the torque ripple. The definition of torque ripple is as follows:

$$Torque\ Ripple\ (\%) = \frac{T_{max} - T_{min}}{T_{avg}} * 100\% \tag{4}$$

where $T_{max}$ is the maximum value of the instantaneous torque waveform, $T_{min}$ is the minimum value, and $T_{avg}$ is the average value. Table 4 shows the range of the input design variables for optimization (see Figure 10a).

**Table 4.** Design variables used in the optimal design and their ranges.

| Design Parameter | Symbol | Range | |
|---|---|---|---|
| | | Min | Max |
| Magnet arc eccentricity radius | $r_{ec}$ | 22.5 mm | 15.5 mm |
| Magnet width ratio | $\tau_{pm}$ | 0.85 | 0.6 |
| Magnet thickness | $h_{pm}$ | 4 mm | 3 mm |
| Slot opening ratio | $b_o$ | 0.55 | 0.35 |
| Slot width ratio | $b_s$ | 0.55 | 0.35 |
| Tooth-tip thickness | $h_{tt}$ | 2.4 mm | 1.2 mm |

Figure 13 shows the proposed optimization process, divided into three steps: (1) Initial setup to define objective functions and constraints, followed by parent sample generation and evaluation through FEA; (2) Construction of the SM employing FE-calculated data until convergence criteria are met; and (3) Surrogate-based optimization utilizing the NSGA-II algorithm. The flowchart in Figure 13 is developed by incorporating the proposed GP-UCB-based adaptive sampling shown in Figure 3b into the surrogate-assisted optimization process introduced in [11]. As shown in the figure, the proposed adaptive sampling is applied to both step 2 and step 3, leveraging the advantages of being applied to each phase.

Figure 14 shows a side-by-side comparison of the initial geometry and optimized design for the 9-slot/6-pole model, showing the changes in tooth width, magnet geometry, and slot openings. Table 5 compares the machine performance before and after optimization, showing improvements across all aspects except torque ripple. Despite the inverse relationship between torque density and losses, the optimized design exhibits a 13% increase in torque density with a slight decrease in losses, and an 11% reduction in cogging torque, from ±7.4 mNm to ±6.6 mNm. Although torque ripple increased from 2.17% to 2.94%, it is still within the targeted 3% constraint. To successfully suppress cogging torque and torque ripple, the step skew technique mentioned earlier was applied to Design 1.

**Table 5.** Performance comparison of the 9-slot/6-pole design before and after optimization.

| | Torque Density [Nm/kg] | Cogging Torque [mNm] | Torque Ripple [%] | Losses [W] | Cost [\$] |
|---|---|---|---|---|---|
| Before opt. | 1.31 | 7.41 | 2.17 | 64.94 | 20.83 |
| After opt. | 1.48 | 6.62 | 2.94 | 63.94 | 19.20 |
| Difference [%] | +12.98 | −10.66 | +35.48 | −1.54 | −8.83 |

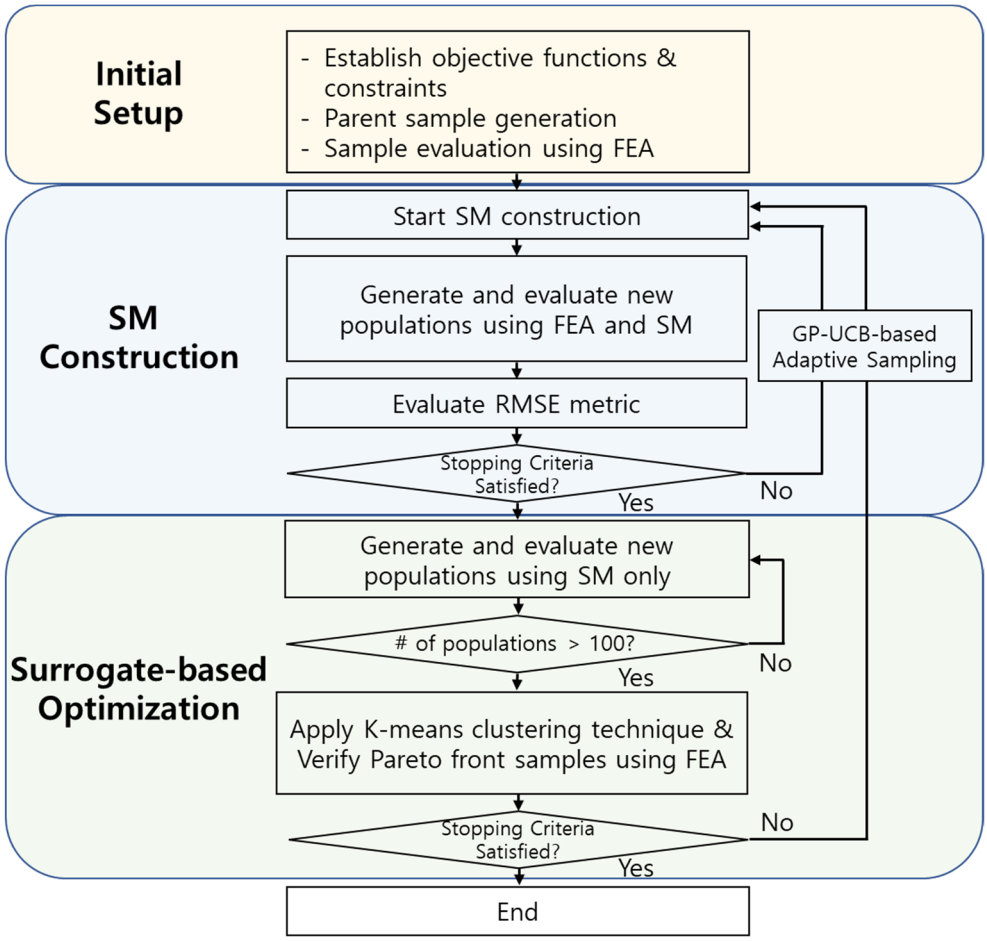


**Figure 13.** Multi-objective design optimization process using GP-UCB-based adaptive sampling.

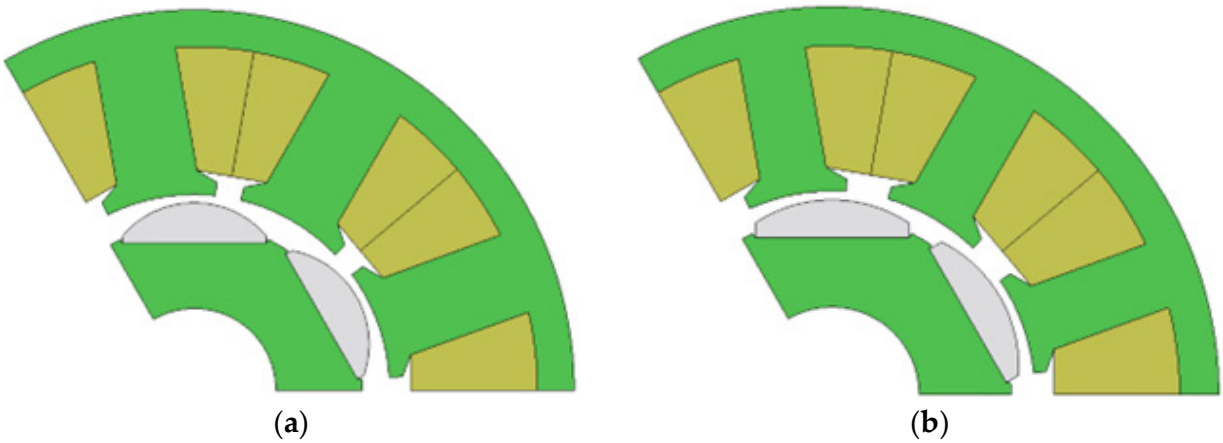


**Figure 14.** Cross sections of Design 1. (**a**) Before optimization, (**b**) after optimization.

Figure 15 shows a comparison of the initial and optimized geometry for the 12/10 model. The optimized design shows a slight change in tooth width, a wider arc angle, and reduced magnet height. Table 6 shows the difference in performance before and after the optimization, showing an overall improvement in performance. Losses increased slightly from 54.5 W to 55.7 W, but torque density increased by 5.2%, and cogging torque plummeted from ±40.1 mNm to ±6.3 mNm without rotor skew, a reduction of 84%. Importantly, for the same operating conditions outlined in Table 3, the 12/10 model had 15% lower losses than the 9/6 model, and achieved similar levels of cogging torque and torque ripple

without applying step skew to the rotor. Torque ripple increased from 2.1% to 2.7%, staying within the targeted 3% constraint. Table 7 provides the change in design parameters before and after optimization for Design 1 and Design 2, respectively.

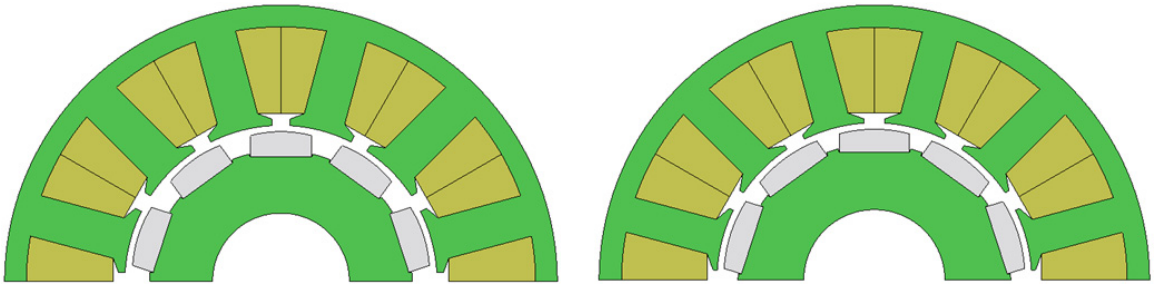

(**a**) (**b**)

**Figure 15.** Cross sections of Design 2. (**a**) Before optimization, (**b**) after optimization.

**Table 6.** Performance comparison of the 12-slot/10-pole design before and after optimization.

| | Torque Density [Nm/kg] | Cogging Torque [mNm] | Torque Ripple [%] | Losses [W] | Cost [$] |
|---|---|---|---|---|---|
| Before opt. | 1.71 | 40.12 | 2.08 | 54.58 | 17.48 |
| After opt. | 1.80 | 6.33 | 2.69 | 55.66 | 16.75 |
| Difference [%] | +5.23 | −84.19 | +29.44 | +1.98 | −4.21 |

**Table 7.** Parameter variations before and after optimization.

| Design Parameter | Symbol | Design 1 | | Design 2 | |
|---|---|---|---|---|---|
| | | Before | After | Before | After |
| Magnet arc eccentricity radius [mm] | $r_{ec}$ | 16 | 16 | 16.5 | 21.4 |
| Magnet width ratio [-] | $\tau_{pm}$ | 0.85 | 0.85 | 0.85 | 0.85 |
| Magnet thickness [mm] | $h_{pm}$ | 4.00 | 4.13 | 4.00 | 3.53 |
| Slot opening ratio [-] | $b_o$ | 0.35 | 0.41 | 0.40 | 0.41 |
| Slot width ratio [-] | $b_s$ | 0.40 | 0.48 | 0.40 | 0.40 |
| Tooth-tip thickness [mm] | $h_{tt}$ | 1.70 | 1.41 | 0.90 | 0.67 |

The NSGA-II algorithm uses a population of 50 and 40 evolutionary generations, with a crossover probability of 0.9 and a mutation probability of 0.05. Figure 16 shows the 3D projections of the Pareto non-dominated designs and the Pareto front for Design 1 and Design 2, illustrating optimal solution sets among conflicting objective functions. Conventional solution-finding methods based on weighting factors are susceptible to biases, elevating the likelihood of obtaining locally optimal solutions. Hence, in modern optimization practices, machine designers often make selections based on technical requirements, strategically navigating tradeoffs among various objective functions. Indeed, considering the nature of muti-objective optimization, achieving a single global solution optimizing all three objective functions simultaneously is unattainable. Our approach involves prioritizing the reduction of cogging torque while balancing other objectives and constraints, aligning with the characteristics of EPS applications. It is worth noting that the displayed samples represent a subset of the total tested, considering the scale of the plot axes.

Table 8 provides the design optimization results for Design 1 and Design 2. In particular, the 12/0 model (Design 2) shows excellent performance characteristics across torque density, efficiency, cost, and manufacturability. Both models exhibit excellent cogging torque characteristics and maintain torque ripple within the targeted 3%, which is consistent with the desirable characteristics for EPS applications.

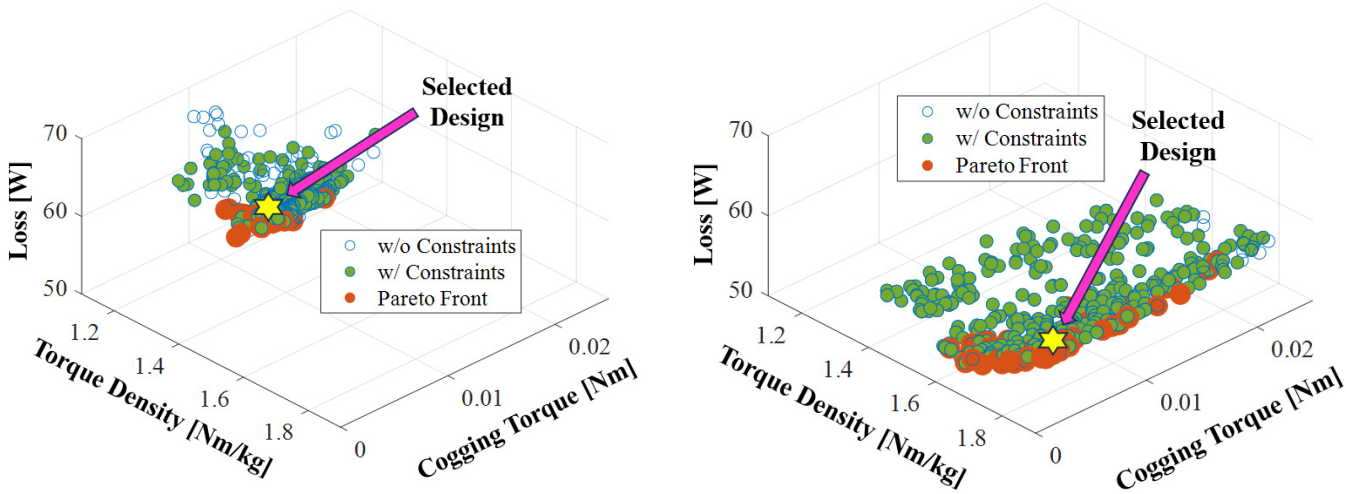


**Figure 16.** 3D objective space projections of the Pareto non-dominated designs and Pareto front. (**a**) Design 1 (9-slot/6-pole), (**b**) Design 2 (12-slot/10-pole).

**Table 8.** Performance comparison between the two baseline designs.

| | Torque Density [Nm/kg] | Cogging Torque [mNm] | Torque Ripple [%] | Losses [W] | Cost [$] | Rotor Skew |
|---|---|---|---|---|---|---|
| Design 1 (9-slot/6-pole) | 1.48 | 6.62 | 2.94 | 63.94 | 19.20 | O |
| Design 2 (12-slot/10-pole) | 1.80 (+22%) | 6.33 (−4%) | 2.69 (−9%) | 55.66 (−13%) | 16.75 (−13%) | X |

Figure 17 presents instantaneous torque waveforms for Design 1 and Design 2 under no load (i.e., cogging torque) and at rated load. The implementation of rotor step skew effectively controls torque ripple to under 3% at the rated condition for Design 1, with cogging torque amplitude sufficiently suppressed to approximately 6 mNm. Design 2, even without rotor step skew, displays comparable torque ripple and cogging torque, suggesting easier and more cost-effective manufacturing.

Finally, efficiency performance is compared between Design 1 and Design 2. Figure 18 illustrates the efficiency maps for the two baseline designs under the conditions outlined in Table 2. Design 2 has a 7.7% higher fundamental winding factor than Design 1, resulting in noticeably lower losses for the same torque. Looking at the operating points (see Table 3) overlaid on the efficiency maps in Figure 18a,b, we can see that Design 2 has a relatively higher operating efficiency.

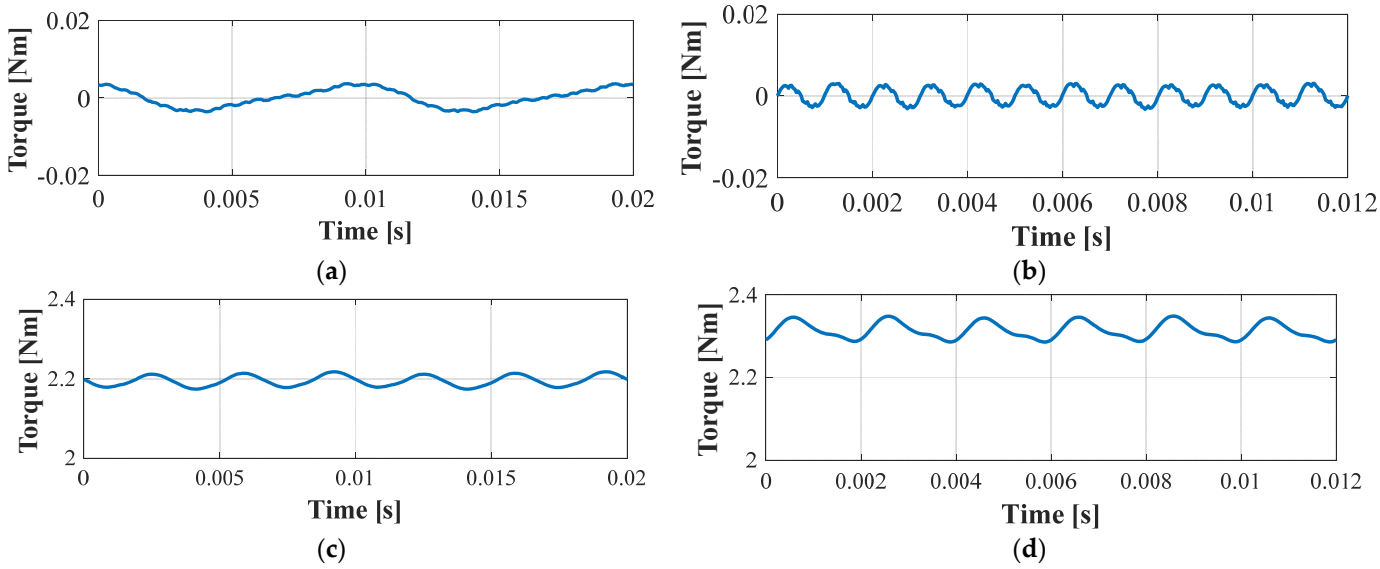


**Figure 17.** Torque waveforms of Design 1 and Design 2. (**a**) Cogging torque waveform for Design 1, (**b**) cogging torque waveform for Design 2, (**c**) torque ripple waveform for Design 1, (**d**) torque ripple waveform for Design 2.

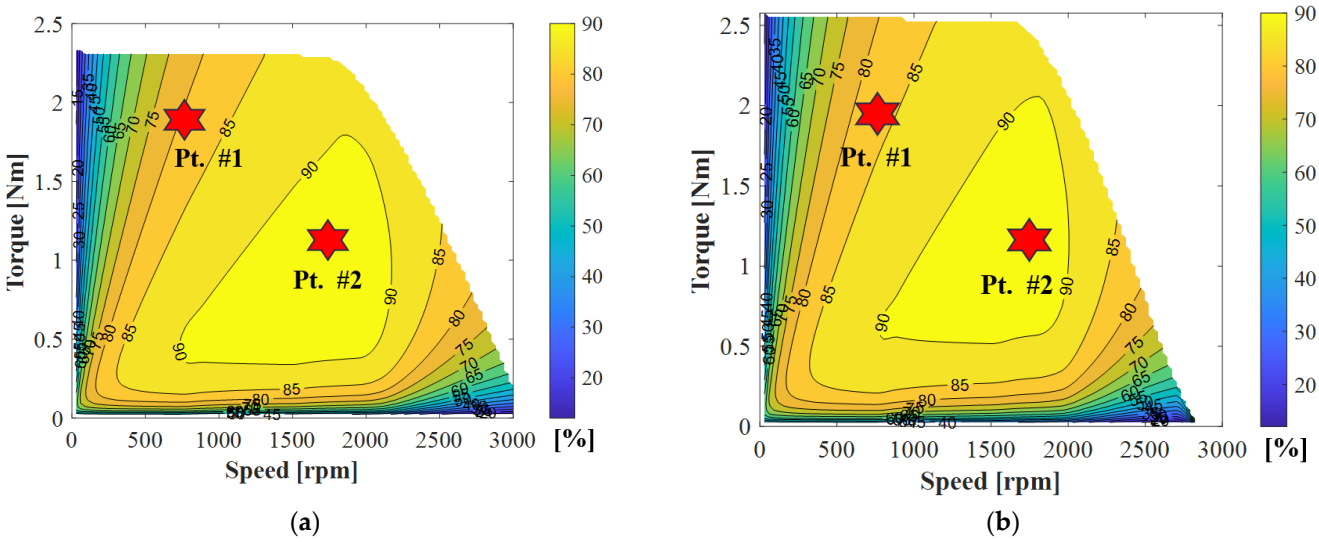


**Figure 18.** Comparison of efficiency maps. (**a**) Design 1, (**b**) Design 2.

## 5. Prototype Machine and Experimental Results

To experimentally validate the performance of Design 2, a prototype machine was built and tested. Figure 19 shows a 200 W (rated) 12-slot/10-pole prototype FSCW-SPM machine specifically designed for EPS application. The rotor in this prototype FSCW-SPM machine features N42SH sintered NdFeB magnets, which have excellent thermal resistance up to 120 °C.

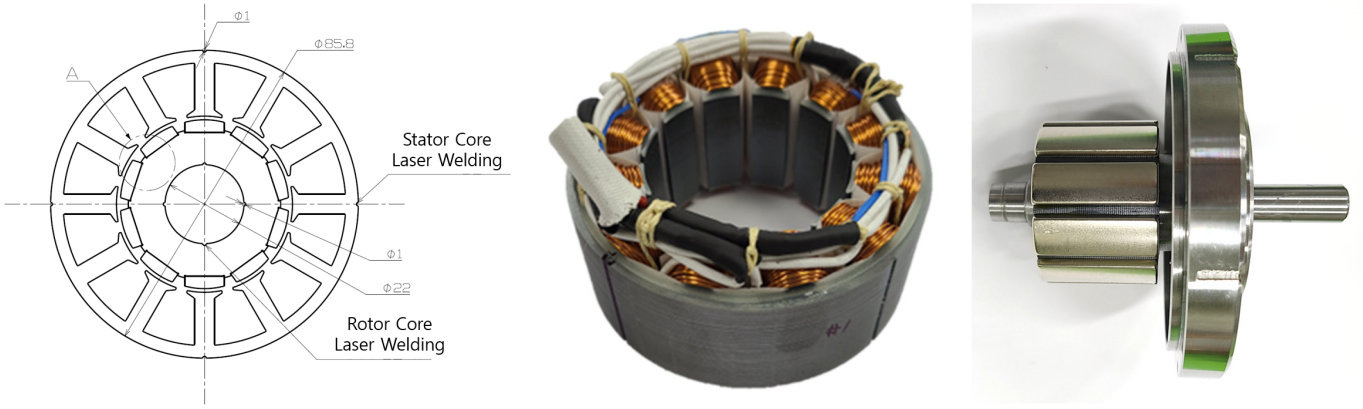


(**a**) (**b**) (**c**)

**Figure 19.** Prototype EPS motor: (**a**) Machine drawing, (**b**) stator core and windings; (**c**) rotor core and magnets with the bearing and front cover attached.

Figure 20a shows the back-to-back dynamometer setup used for testing. The prototype machine was mounted on the dynamometer and an industrial SPM machine with a maximum torque of 4.8 Nm, and a maximum speed of 5000 rpm was used as a prime mover to perform back-emf voltage testing at no-load. This dynamometer setup is controlled by a custom dual-inverter motor drive, as shown in Figure 20b.

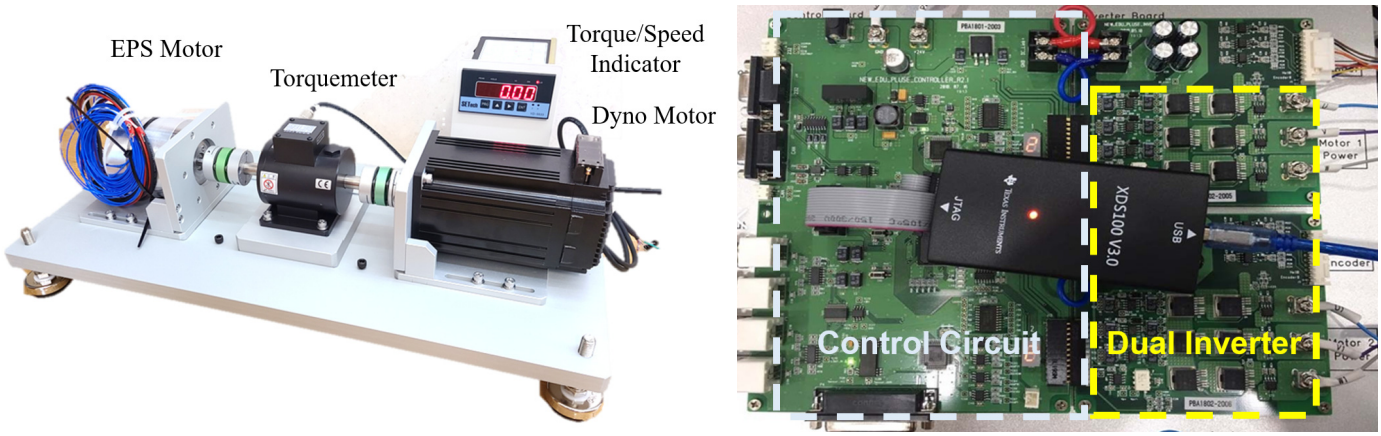


(**a**) (**b**)

**Figure 20.** Experimental dynamometer setup. (**a**) Dynamometer jig, (**b**) inverter hardware.

Table 9 summarizes the experimental reverse electromotive force voltage measurement results. Figure 21 provides a comparison between the measured back-emf voltage waveform and the FE-predicted back-emf waveform. As evident in the figure, the measured waveform closely matches the FE predicted waveform, indicating excellent agreement. Figure 22 shows a comparison of the FFT spectra of the FE-predicted waveform and measured back-emf waveform. The resulting calculated THD values are 1.94% for the simulated result and 1.38% for the experimental result, indicating that both waveforms are very close to the ideal sinusoidal waveform.

**Table 9.** A comparison of measured and FE-predicted phase back-emf voltages at 1000 RPM.

| Test Type | Phase-*a* | Phase-*b* | Phase-*c* | Average |
|---|---|---|---|---|
| Experiment | 11.24 Vrms | 11.24 Vrms | 11.21 Vrms | 11.23 Vrms |
| FEA | 11.20 Vrms | 11.20 Vrms | 11.20 Vrms | 11.20 Vrms |

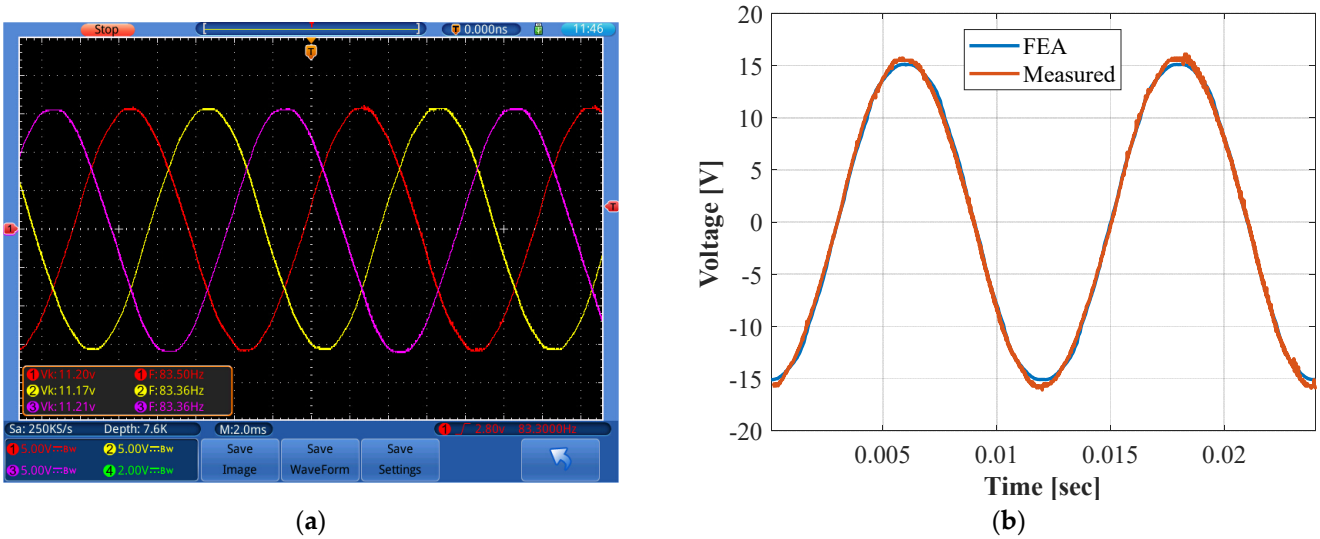


(**a**) (**b**)

**Figure 21.** Back-emf waveforms of the prototype FSCW-SPM machine. (**a**) Measured back-emf voltage waveforms, (**b**) measured vs. FE-predicted back-emf waveforms.

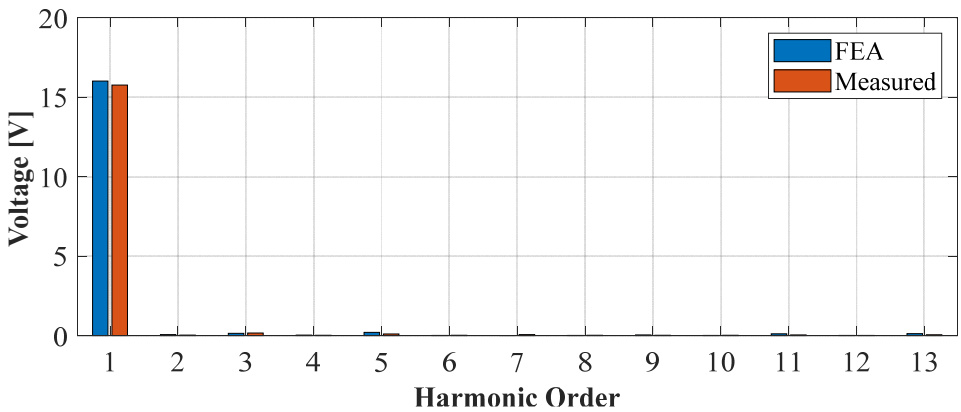


**Figure 22.** FFT spectrum comparison: FEA vs. measured back-emf waveforms.

## 6. Conclusions

This paper presented a novel design optimization process utilizing GP-UCB-based adaptive sampling for electric machine design. Through two case studies involving an IPMSM for EV applications and an FSCW-SPMSM for EPS applications, the proposed approach demonstrated superior performance compared to conventional optimization methods lacking adaptive sampling. Specifically, the adaptive sampling technique significantly improved key optimization performance measures, including exploitation–exploration balance, convergence speed, sensitivity to initial sampling, and repeatability.

Subsequently, GP-UCB-based adaptive sampling was employed in the optimization process to identify the optimal design for EPS applications with demanding performance requirements. The results highlighted that an FSCW-SPM design featuring a 12-slot/10-pole configuration exhibited exceptional torque density, high efficiency, low cost, and enhanced manufacturability—aligning well with the desired performance characteristics for EPS applications. The optimization results were further validated through a dynamometer test, revealing an error of only 0.3% between the amplitude of measured and simulated back-emf voltages, indicating excellent agreement.

Finally, it was shown that the proposed approach is applicable to various stator and rotor configurations with minimal modifications. Categorized as a black-box approach, the proposed method exhibits certain limitations compared to a model-based approach. These include a lack of physical insights, limited control over the algorithm's decision-making

process, and the need for intensive computational resources. It is up to the judgment of the machine designer to strike a balance between different approaches to improve the efficiency and physical significance of the design process. Planned future work includes further experimental validation under different loading conditions and evaluation of a broader range of optimization algorithms and sampling techniques for different types of electric machines.

**Author Contributions:** Methodology, software, formal analysis, validation, data curation, writing—original draft preparation, writing—review and editing, supervision, G.C.; software, formal analysis, G.-H.J.; methodology, software, formal analysis, writing—review, M.C.; validation, data curation, J.K.; formal analysis, writing—review, Y.G.K.; conceptualization, funding acquisition, writing—review and editing, S.K. All authors have read and agreed to the published version of the manuscript.

**Funding:** This work was supported in part by the NRF (National Research Foundation) grant funded by the Korean government (MSIT: Ministry of Science and ICT) (grant number: 2021R1F1A1048754), and in part by the Education and Research Promotion Program of KOREATECH in 2023.

**Data Availability Statement:** Data are contained within the article.

**Conflicts of Interest:** The authors declare no conflicts of interest.

## References

1. Bianchi, N.; Bolognani, S. Design techniques for reducing the cogging torque in surface-mounted PM motors. *IEEE Trans. Ind. Appl.* **2002**, *38*, 1259–1265. [CrossRef]
2. Bianchi, N.; Pre, M.D.; Bolognani, S. Design of a fault-tolerant IPM motor for electric power steering. *IEEE Trans. Veh. Technol.* **2006**, *55*, 1102–1111. [CrossRef]
3. Jang, J.; Cho, S.G.; Lee, S.J.; Kim, K.S.; Kim, J.M.; Hong, J.P.; Lee, T.H. Reliability-Based Robust Design Optimization with Kernel Density Estimation for Electric Power Steering Motor Considering Manufacturing Uncertainties. *IEEE Trans. Magn.* **2015**, *51*, 8001904. [CrossRef]
4. Naidu, M.; Gopalakrishnan, S.; Nehl, T.W. Fault-Tolerant Permanent Magnet Motor Drive Topologies for Automotive X-By-Wire Systems. *IEEE Trans. Ind. Appl.* **2010**, *46*, 841–848. [CrossRef]
5. Uler, G.F.; Mohammed, O.A.; Koh, C.-S. Design optimization of electrical machines using genetic algorithms. *IEEE Trans. Magn.* **1995**, *31*, 2008–2011. [CrossRef]
6. Gao, J.; Sun, H.; He, L.; Dong, Y.; Zheng, Y. Optimization design of Switched Reluctance Motor based on Particle Swarm Optimization. In Proceedings of the 2011 International Conference on Electrical Machines and Systems, Beijing, China, 20–23 August 2011; pp. 1–5. [CrossRef]
7. Mutluer, M.; Bilgin, O. Design optimization of PMSM by particle swarm optimization and genetic algorithm. In Proceedings of the 2012 International Symposium on Innovations in Intelligent Systems and Applications, Trabzon, Turkey, 2–4 July 2012; pp. 1–4. [CrossRef]
8. Duan, Y.; Harley, R.G.; Habetler, T.G. Comparison of Particle Swarm Optimization and Genetic Algorithm in the design of permanent magnet motors. In Proceedings of the 2009 IEEE 6th International Power Electronics and Motion Control Conference, Wuhan, China, 17–20 May 2009; pp. 822–825. [CrossRef]
9. Murata, T.; Ishibuchi, H. MOGA: Multi-objective genetic algorithms. In Proceedings of the 1995 IEEE International Conference on Evolutionary Computation, Perth, WA, Australia, 29 November–1 December 1995; pp. 289–294. [CrossRef]
10. Li, Y.; Lei, G.; Bramerdorfer, G.; Peng, S.; Sun, X.; Zhu, J. Machine Learning for Design Optimization of Electromagnetic Devices: Recent Developments and Future Directions. *Appl. Sci.* **2021**, *11*, 1627. [CrossRef]
11. Choi, M.; Choi, G.; Bramerdorfer, G.; Marth, E. Systematic Development of a Multi-Objective Design Optimization Process Based on a Surrogate-Assisted Evolutionary Algorithm for Electric Machine Applications. *Energies* **2023**, *16*, 392. [CrossRef]
12. Taran, N.; Ionel, D.M.; Dorrell, D.G. Two-Level Surrogate-Assisted Differential Evolution Multi-Objective Optimization of Electric Machines Using 3-D FEA. *IEEE Trans. Magn.* **2018**, *54*, 8107605. [CrossRef]
13. Gao, Y.; Yang, T.; Bozhko, S.; Wheeler, P.; Dragičević, T. Filter Design and Optimization of Electromechanical Actuation Systems Using Search and Surrogate Algorithms for More-Electric Aircraft Applications. *IEEE Trans. Transp. Electrif.* **2020**, *6*, 1434–1447. [CrossRef]
14. Gu, J.; Hua, W.; Yu, W.; Zhang, Z.; Zhang, H. Surrogate Model-Based Multiobjective Optimization of High-Speed PM Synchronous Machine: Construction and Comparison. *IEEE Trans. Transp. Electrif.* **2023**, *9*, 678–688. [CrossRef]
15. Yoo, C.-H. A New Multi-Modal Optimization Approach and Its Application to the Design of Electric Machines. *IEEE Trans. Magn.* **2018**, *54*, 8202004. [CrossRef]
16. Jackson, D.; Belakaria, S.; Cao, Y.; Doppa, J.R.; Lu, X. Machine Learning Enabled Design Automation and Multi-Objective Optimization for Electric Transportation Power Systems. *IEEE Trans. Transp. Electrif.* **2022**, *8*, 1467–1481. [CrossRef]

17. Gupta, S.; Biswas, P.K.; Debnath, S.; Ghosh, A.; Babu, T.S.; Zawbaa, H.M.; Kamel, S. Metaheuristic Optimization Techniques Used in Controlling of an Active Magnetic Bearing System for High-Speed Machining Application. *IEEE Access* **2023**, *11*, 12100–12118. [CrossRef]
18. Eason, J.; Cremaschi, S. Adaptive sequential sampling for surrogate model generation with artificial neural networks. *Comput. Chem. Eng.* **2014**, *68*, 220–232. [CrossRef]
19. Fushiki, T. Estimation of prediction error by using K-fold cross-validation. *Stat. Comput.* **2011**, *21*, 137–146. [CrossRef]
20. Meckesheimer, M.; Booker, A.J.; Barton, R.R.; Simpson, T.W. Computationally inexpensive metamodel assessment strategies. *AIAA J.* **2002**, *40*, 2053–2060. [CrossRef]
21. Jiang, C.; Cai, X.; Qiu, H.; Gao, L.; Li, P. A two-stage support vector regression assisted sequential sampling approach for global metamodeling. *Struct. Multidiscip. Optim.* **2018**, *58*, 1657–1672. [CrossRef]
22. Fuhg, J.N.; Fau, A.; Nackenhorst, U. State-of-the-Art and Comparative Review of Adaptive Sampling Methods for Kriging. *Arch. Comput. Methods Eng.* **2021**, *28*, 2689–2747. [CrossRef]
23. Liu, H.; Xu, S.; Wang, X.; Wu, J.; Song, Y. A global optimization algorithm for simulation-based problems via the extended DIRECT scheme. *Eng. Optim.* **2015**, *47*, 1441–1458. [CrossRef]
24. Burke, J.V.; Curtis, F.E.; Lewis, A.S.; Overton, M.L.; Simões, L.E.A. Gradient Sampling Methods for Nonsmooth Optimization. *arXiv* **2018**. [CrossRef]
25. Sóbester, A.; Leary, S.J.; Keane, A.J. On the design of optimization strategies based on global response surface approximation models. *J. Glob. Optim.* **2005**, *33*, 31–59. [CrossRef]
26. Kleijnen, J.P.C.; Van Beers, W.C.M. Application-driven sequential designs for simulation experiments: Kriging metamodeling. *J. Oper. Res. Soc.* **2004**, *55*, 876–883. [CrossRef]
27. Liu, H.; Xu, S.; Ma, Y.; Chen, X.; Wang, X. An Adaptive Bayesian Sequential Sampling Approach for Global Metamodeling. *J. Mech. Des.* **2016**, *138*, 011404. [CrossRef]
28. Nuchitprasittichai, A.; Cremaschi, S. An algorithm to determine sample sizes for optimization with artificial neural networks. *AIChE J.* **2013**, *59*, 805–812. [CrossRef]
29. Makondo, N.; Folarin, A.L.; Zitha, S.N.; Remy, S.L. An Analysis of Reinforcement Learning for Malaria Control. *arXiv* **2021**. [CrossRef]
30. Choi, M.; Choi, G. Investigation, and Mitigation of AC Losses in IPM Machines with Hairpin Windings for EV Applications. *Energies* **2021**, *14*, 8034. [CrossRef]
31. Agushaka, J.O.; Ezugwu, A.E. Initialisation Approaches for Population-Based Metaheuristic Algorithms: A Comprehensive Review. *Appl. Sci.* **2022**, *12*, 896. [CrossRef]
32. EL-Refaie, A.M. Fractional-Slot Concentrated-Windings Synchronous Permanent Magnet Machines: Opportunities and Challenges. *IEEE Trans. Ind. Electron.* **2010**, *57*, 107–121. [CrossRef]
33. Cros, J.; Viarouge, P. Synthesis of high performance PM motors with concentrated windings. *IEEE Trans. Energy Convers.* **2002**, *17*, 248–253. [CrossRef]
34. Choi, G.; Jahns, T.M. Analysis and Design Recommendations to Mitigate Demagnetization Vulnerability in Surface PM Synchronous Machines. *IEEE Trans. Ind. Appl.* **2018**, *54*, 1292–1301. [CrossRef]